A Lightweight RK4-Based Wheel Odometry Integration for OpenVINS

Mehmet Muratoglu[1] and Ismail Uyanik[2]

Abstract— **This paper presents a real-world validation of the OpenVINS visual–inertial odometry framework on a custom wheeled mobile robot equipped with a stereo camera, an IMU, and wheel encoders. We additionally introduce a lightweight wheel-odometry integration method that preserves the original OpenVINS MSCKF architecture. Inspired by the RK4-based motion integration strategy used in MINS, the method converts wheel measurements into relative-motion constraints and incorporates them during the filter update without augmenting the estimator state. This design retains the computational profile of standard OpenVINS while providing complementary motion information when visual tracking degrades because of motion blur, low texture, repetitive structure, or illumination changes. Experiments on representative closed-loop trajectories show that the wheel-assisted configuration yields more stable estimates and reduced drift relative to baseline OpenVINS, with the clearest gains in visually challenging sequences. The results indicate that lightweight wheel assistance can improve the practical robustness of OpenVINS for deployable ground robots.**

I. INTRODUCTION

Visual–inertial odometry (VIO) is a key capability for mobile robots operating in GPS-denied environments because it combines the complementary strengths of cameras and inertial sensors. Cameras provide rich geometric information about the scene, while inertial measurements supply high-rate motion cues during rapid maneuvers and brief visual dropouts. This combination enables metric motion estimation for navigation, mapping, obstacle avoidance, and control on compact embedded platforms. Among practical VIO formulations, the multi-state constraint Kalman filter (MSCKF) [1] remains attractive because it offers a favorable balance between estimation accuracy and computational cost. OpenVINS [2] , which builds on this formulation, has therefore become a useful open-source platform for both research and deployment. Validating OpenVINS on real hardware is important not only to characterize nominal performance, but also to expose timing, calibration, vibration, and platform-specific effects that often appear only in field operation.

Despite its strengths, pure VIO remains sensitive to several common failure modes. Motion blur, low-texture scenes, repetitive structure, illumination changes, and transient occlusions can reduce the number and quality of tracked features [3], while IMU bias and noise accumulate into drift over long trajectories [4] . These effects are especially problematic on wheeled ground robots [5] , whose motion often consists of prolonged straight segments, brief stops, and gentle turns that provide limited excitation for the estimator. As a result, the most informative validation scenarios are often the ones in which baseline OpenVINS becomes fragile rather than nominally easy trajectories.

Wheel odometry provides complementary motion information in exactly these situations. Encoder-based measurements are inexpensive, widely available on ground robots, and informative about short-term translation and heading change even when visual tracking degrades. For this reason, several studies have fused wheel measurements with visual–inertial estimation through tightly coupled optimization and online calibration [6]–[8], motion models and constraints tailored to wheeled platforms [9], and broader multisensor frameworks such as MINS [10]. The challenge is that improved robustness often comes at the cost of higher estimator complexity through state augmentation, additional calibration variables, or heavier back-end computation. For deployable robotic systems, preserving real-time performance is often as important as improving estimation accuracy.

This paper addresses that trade-off with a lightweight wheel-odometry integration strategy for OpenVINS. Inspired by the RK4-based motion integration used in MINS [10], the proposed method converts wheel measurements into relative-motion constraints between consecutive OpenVINS clones and incorporates them during the filter update without augmenting the estimator state. In this way, the original MSCKF structure and computational profile of OpenVINS are preserved, while the estimator gains additional motion information when visual measurements become weak or unreliable.

The contributions of this work are threefold. First, we provide a real-hardware validation of baseline OpenVINS on a custom wheeled robot equipped with a stereo camera, an IMU, and wheel encoders. Second, we introduce an RK4-based wheel-odometry update that is compatible with the original OpenVINS state representation and does not require estimator-state augmentation. Third, we compare the baseline and wheel-assisted configurations on indoor and outdoor closed-loop trajectories to assess improvements in trajectory consistency, drift behavior, and robustness under representative operating conditions.

The remainder of the paper is organized as follows. Section II describes the sensor system and calibration procedure. Section III presents the proposed RK4-based wheel integration method. Section IV describes the experimental setup. Section V reports the comparative results, and Section VI concludes the paper.

[1] Mehmet Muratoglu is with the Department of Computer Engineering, Hacettepe Universtiy, Ankara, Türkiye, mehmetmuratoglu@hacettepe.edu.tr

[2] Ismail Uyanık is with the Department of Electrical and Electronics Engineering, Hacettepe Universtiy, Ankara, Türkiye, ismailuyanik@hacettepe.edu.tr

Fig. 1. Sensor suite used in the experiments.

II. Sensor System

To validate baseline OpenVINS and the proposed wheel-assisted variant, a compact sensor suite was mounted on the robot. The system consists of a ZED X stereo camera [11], an Xsens MTi-7 IMU [12], and an NVIDIA Jetson Orin NX for onboard logging and computation. The sensor suite is shown in Fig. 1, and the main hardware specifications are summarized in Table I.

TABLE I
Main sensor specifications

Component	Specification
Stereo Camera: ZED X	
Resolution	1920×1200 per eye
Lens	4 mm
Frame rate	30 fps
Shutter	Global shutter
Interface	GMSL2
IMU: Xsens MTi-7	
Sensors	3-axis accelerometer, gyroscope, magnetometer
Output rate	100 Hz

Vision and Inertial Sensors

The ZED X stereo camera operates at 30 fps with a global shutter, which helps reduce motion-induced image distortion. The Xsens MTi-7 provides accelerometer and gyroscope measurements at 100 Hz and serves as the inertial input to OpenVINS. IMU noise parameters were identified offline using Allan variance analysis [13] and used to configure the estimator noise model.

Wheel Odometry Source

The sensor module itself does not include wheel encoders. Instead, wheel-based odometry is obtained from the host robot through a ROS 2 `nav_msgs/Odometry` topic. This estimate is generated online by the `robot_localization` EKF [14], which fuses wheel encoder and IMU measurements. In the proposed system, this odometry provides the auxiliary motion input used by the wheel-assisted OpenVINS update.

Calibration and Data Collection

Camera–IMU spatial and temporal calibration was performed offline using Kalibr [15]. All data streams, including stereo images, raw IMU measurements, and fused wheel odometry, were recorded on the Jetson Orin NX using ROS 2 and replayed offline for repeatable evaluation.

III. Methodology

A. Frames and Calibration

Following the OpenVINS convention, we denote the global (inertial) frame by $\mathscr{G}$, the IMU body frame by $\mathscr{B}$, the camera frame by $\mathscr{C}$, and the wheel-odometry frame by $\mathscr{O}$. The camera–IMU extrinsic calibration is represented as

$$ {}^{\mathscr{B}}\mathbf{T}_{\mathscr{C}} = \begin{bmatrix} {}^{\mathscr{B}}\mathbf{R}_{\mathscr{C}} & {}^{\mathscr{B}}\mathbf{p}_{\mathscr{C}} \\ \mathbf{0}_{1\times3} & 1 \end{bmatrix} \tag{1} $$

where ${}^{\mathscr{B}}\mathbf{R}_{\mathscr{C}} \in SO(3)$ and ${}^{\mathscr{B}}\mathbf{p}_{\mathscr{C}} \in \mathbb{R}^3$. A constant temporal offset between the camera and IMU clocks is denoted by $\Delta t_{\mathscr{C}\mathscr{B}}$. These parameters are obtained offline using Kalibr and are treated as fixed during estimation.

Wheel odometry is referenced to frame $\mathscr{O}$. The rigid transform between the IMU and odometry frames is

$$ {}^{\mathscr{O}}\mathbf{T}_{\mathscr{B}} = \begin{bmatrix} {}^{\mathscr{O}}\mathbf{R}_{\mathscr{B}} & {}^{\mathscr{O}}\mathbf{p}_{\mathscr{B}} \\ \mathbf{0}_{1\times3} & 1 \end{bmatrix}, \tag{2} $$

with ${}^{\mathscr{O}}\mathbf{R}_{\mathscr{B}}$ and ${}^{\mathscr{O}}\mathbf{p}_{\mathscr{B}}$ obtained from offline calibration and kept constant throughout the experiments.

B. Wheel Odometry Model

We consider a wheeled robot operating primarily on planar surfaces [9]. The odometry source provides linear and angular velocity estimates, expressed in the IMU frame, as

$$ {}^{\mathscr{B}}\mathbf{v}_w(t) = [v_x, v_y, v_z]^\top, \qquad {}^{\mathscr{B}}\omega_w(t) = [\omega_x, \omega_y, \omega_z]^\top. \tag{3} $$

For differential-drive or skid-steer robots, the dominant terms are typically the forward velocity v_x and yaw rate ω_z [9]. Nevertheless, the full 3-D twist is retained to remain consistent with the IMU-centric estimator state.

Assuming a rigid transform between the IMU and the odometry reference point, wheel measurements are modeled as noisy observations of the IMU body twist:

$$ {}^{\mathscr{B}}\mathbf{v}_w(t) = {}^{\mathscr{B}}\mathbf{v}(t) + \left[{}^{\mathscr{B}}\omega(t)\right]_\times {}^{\mathscr{B}}\mathbf{p}_o + \mathbf{n}_v(t), \tag{4} $$

$$ {}^{\mathscr{B}}\omega_w(t) = {}^{\mathscr{B}}\omega(t) + \mathbf{n}_\omega(t), \tag{5} $$

where ${}^{\mathscr{B}}\mathbf{p}_o$ is the lever arm between the IMU and the odometry reference point, $[\cdot]_\times$ denotes the skew-symmetric matrix, and $\mathbf{n}_v$, $\mathbf{n}_\omega$ are zero-mean measurement noise terms.

C. RK4 Wheel Preintegration

Let t_i and t_j denote two consecutive clone times in the MSCKF sliding window [1]. All wheel measurements in the interval $[t_i, t_j]$ are integrated to form a relative motion increment [16]

$$\Delta \mathbf{T}_{ij} = \begin{bmatrix} \Delta \mathbf{R}_{ij} & \Delta \mathbf{p}_{ij} \\ \mathbf{0}_{1\times 3} & 1 \end{bmatrix} \in SE(3), \tag{6}$$

where $\Delta \mathbf{R}_{ij} \in SO(3)$ and $\Delta \mathbf{p}_{ij} \in \mathbb{R}^3$. which represents the odometry-frame motion at time t_j relative to time t_i.

To reduce integration error during high-rate motion, the relative motion is computed using fourth-order Runge–Kutta (RK4) integration [17]. At the start of each preintegration interval, the relative state is initialized as

$$\Delta \mathbf{q}_i = [0,0,0,1]^\top, \qquad \Delta \mathbf{p}_i = \mathbf{0}, \tag{7}$$

where $\Delta \mathbf{q}$ is the quaternion corresponding to $\Delta \mathbf{R}$.

For each wheel measurement interval $[t_k, t_{k+1}]$, with $\Delta t = t_{k+1} - t_k$, the measured velocities are linearly interpolated as

$$\omega(\tau) = \omega_k + \frac{\omega_{k+1} - \omega_k}{\Delta t}\tau, \qquad \mathbf{v}(\tau) = \mathbf{v}_k + \frac{\mathbf{v}_{k+1} - \mathbf{v}_k}{\Delta t}\tau, \tag{8}$$

for $\tau \in [0, \Delta t]$.

The rotational and translational dynamics are

$$f_q(\mathbf{q}, \omega) = \frac{1}{2}\Omega(\omega)\mathbf{q}, \qquad f_p(\mathbf{q}, \mathbf{v}) = \mathbf{R}(\mathbf{q})^\top \mathbf{v}, \tag{9}$$

where $\Omega(\cdot)$ is the standard quaternion rate matrix and $\mathbf{R}(\mathbf{q})$ is the rotation corresponding to quaternion $\mathbf{q}$.

Using midpoint values

$$\bar{\omega}_k = \frac{\omega_k + \omega_{k+1}}{2}, \qquad \bar{\mathbf{v}}_k = \frac{\mathbf{v}_k + \mathbf{v}_{k+1}}{2}, \tag{10}$$

the RK4 stages are

$$\begin{aligned}
\mathbf{k}_1^q &= f_q(\Delta \mathbf{q}_k, \omega_k), & \mathbf{k}_1^p &= f_p(\Delta \mathbf{q}_k, \mathbf{v}_k), \\
\mathbf{k}_2^q &= f_q\left(\Delta \mathbf{q}_k + \frac{\Delta t}{2}\mathbf{k}_1^q, \bar{\omega}_k\right), & \mathbf{k}_2^p &= f_p\left(\Delta \mathbf{q}_k + \frac{\Delta t}{2}\mathbf{k}_1^q, \bar{\mathbf{v}}_k\right), \\
\mathbf{k}_3^q &= f_q\left(\Delta \mathbf{q}_k + \frac{\Delta t}{2}\mathbf{k}_2^q, \bar{\omega}_k\right), & \mathbf{k}_3^p &= f_p\left(\Delta \mathbf{q}_k + \frac{\Delta t}{2}\mathbf{k}_2^q, \bar{\mathbf{v}}_k\right), \\
\mathbf{k}_4^q &= f_q\left(\Delta \mathbf{q}_k + \Delta t\, \mathbf{k}_3^q, \omega_{k+1}\right), & \mathbf{k}_4^p &= f_p\left(\Delta \mathbf{q}_k + \Delta t\, \mathbf{k}_3^q, \mathbf{v}_{k+1}\right).
\end{aligned} \tag{11}$$

The preintegrated state is then updated as

$$\Delta \mathbf{q}_{k+1} = \text{normalize}\left(\Delta \mathbf{q}_k + \frac{\Delta t}{6}\left(\mathbf{k}_1^q + 2\mathbf{k}_2^q + 2\mathbf{k}_3^q + \mathbf{k}_4^q\right)\right), \tag{12}$$

$$\Delta \mathbf{p}_{k+1} = \Delta \mathbf{p}_k + \frac{\Delta t}{6}\left(\mathbf{k}_1^p + 2\mathbf{k}_2^p + 2\mathbf{k}_3^p + \mathbf{k}_4^p\right). \tag{13}$$

Accumulating these updates over all wheel samples between t_i and t_j yields the relative increment $(\Delta \mathbf{R}_{ij}, \Delta \mathbf{p}_{ij})$.

D. Covariance Propagation and MSCKF Update

The uncertainty of the preintegrated wheel motion is modeled using the 6-DoF error state [17]

$$\delta \mathbf{x} = \begin{bmatrix} \delta\theta \\ \delta \mathbf{p} \end{bmatrix}, \qquad \mathbf{n} = \begin{bmatrix} \mathbf{n}_\omega \\ \mathbf{n}_v \end{bmatrix}. \tag{14}$$

where $\delta\theta \in \mathbb{R}^3$ is the $SO(3)$ tangent-space rotation error and $\delta \mathbf{p} \in \mathbb{R}^3$ is the additive position error of the preintegrated motion. Its discrete-time propagation is

$$\delta \mathbf{x}_{k+1} = \mathbf{F}_k \delta \mathbf{x}_k + \mathbf{G}_k \mathbf{n}_k, \tag{15}$$

$$\mathbf{P}_{k+1} = \mathbf{F}_k \mathbf{P}_k \mathbf{F}_k^\top + \mathbf{G}_k \mathbf{Q}_k \mathbf{G}_k^\top, \tag{16}$$

with

$$\mathbf{F}_k = \begin{bmatrix} \Delta R_k (\Delta R_{k-1})^\top & 0 \\ -[\Delta p_k - \Delta p_{k-1}]_\times & I_3 \end{bmatrix}, \qquad \mathbf{G}_k = \begin{bmatrix} I_3 \Delta t & 0 \\ 0 & (\Delta R_{k-1})^\top \Delta t \end{bmatrix} \tag{17}$$

The preintegrated motion is used as a relative measurement between clone states. Let $(\mathbf{R}_{ij}^{\text{est}}, \mathbf{p}_{ij}^{\text{est}})$ denote the relative motion predicted by the current MSCKF state. The wheel residual is then

$$\mathbf{r}_{\text{wheel}} = \begin{bmatrix} -\operatorname{Log}\left(\Delta R_{ij} \, (R_{ij}^{est})^\top\right) \\ \Delta p_{ij} - p_{ij}^{est} \end{bmatrix} \tag{18}$$

The corresponding Jacobians are computed using the first-estimate Jacobian (FEJ) principle [18], [19] to preserve filter consistency. This residual is injected into OpenVINS as a standard MSCKF update, allowing wheel information to improve robustness without augmenting the estimator state.

IV. Experimental Setup

The proposed wheel-assisted OpenVINS system was evaluated on a custom wheeled mobile robot in both indoor and outdoor environments. The experiments were designed to examine estimator behavior under different visual conditions and motion profiles, including visually challenging corridor navigation and feature-rich outdoor operation. For fair comparison, the baseline OpenVINS configuration and the proposed wheel-assisted configuration were both executed offline using the same recorded ROS 2 bag files. In this way, both pipelines processed identical stereo, IMU, and wheel-odometry inputs.

The evaluation included three representative scenarios: an indoor corridor run, an outdoor straight-line run, and an outdoor free-form trajectory. The indoor and free-form outdoor runs were performed on paths that returned approximately to the starting location, allowing the consistency of the estimated trajectory to be inspected visually from the start–end alignment. Since OpenVINS was used in odometry mode, this behavior reflects estimator drift rather than explicit loop-closure correction. When a reference trajectory was available, standard trajectory error metrics were additionally reported. The experiments covered typical ground-robot motion, including straight segments, turns, and short stops, with run durations of approximately 5–10 minutes.

Fig. 2. Custom wheeled mobile robot platform used in the experiments.

A. Robot Platform

The experiments were conducted on a four-wheeled skid-steer mobile robot measuring 280 mm in width and 650 mm in length, with 140 mm diameter wheels. Each wheel is actuated by a brushless DC motor equipped with quadrature encoders. Encoder measurements are processed by an ESP32 microcontroller and transmitted to the Jetson Orin NX through micro-ROS [20]. On the Jetson, the `robot_localization` package [14] fuses wheel encoder and IMU measurements using an EKF to produce the odometry stream used by the proposed method.

The sensor module described in Section II is rigidly mounted on the robot chassis. The ZED X stereo camera faces forward, and the Xsens MTi-7 IMU is mounted in close proximity to reduce lever-arm effects. The complete experimental platform is shown in Fig. 2.

B. Indoor Corridor Scenario

The indoor experiment was carried out in a corridor environment, shown in Fig. 3. Such environments are challenging for visual–inertial odometry because walls and floors often contain repetitive structure and limited distinctive texture. As a result, feature tracking can become less reliable, increasing the likelihood of accumulated drift. This scenario was therefore selected to assess the benefit of wheel odometry under weak visual conditions.

Both the baseline and wheel-assisted configurations completed the indoor run without tracking failure.

C. Outdoor Scenarios

The outdoor experiments were conducted on a flat concrete surface under natural lighting, as shown in Fig. 4. Compared with the indoor corridor, the outdoor scene provides richer texture and a larger number of distinctive visual features, which generally improves feature tracking and benefits visual–inertial estimation.

Two outdoor tests were considered. The first was a straight-line run for which a reference trajectory was available, enabling quantitative comparison. The second was a free-form path without external ground truth, evaluated qualitatively through the geometric consistency of the estimated trajectory. Both configurations completed the outdoor experiments without tracking failure.

V. Results and Validation

This section compares the baseline OpenVINS estimator with the proposed wheel-assisted OpenVINS configuration. When a reference trajectory was available, performance was evaluated using standard trajectory error metrics: root mean square error (RMSE), mean absolute pose error (Mean APE), maximum absolute pose error (Max APE), and mean relative pose error (Mean RPE). For sequences without external reference, the comparison is based on the geometric consistency of the estimated trajectory and its final alignment with the starting point.

A. Indoor Corridor Results

The quantitative results for the indoor corridor experiment are summarized in Table II. In this visually challenging environment, the wheel-assisted configuration improves performance across all reported metrics.

TABLE II

Trajectory error metrics for the indoor experiment

Method	RMSE	Mean APE	Max APE	Mean RPE
OpenVINS	1.3445	1.1030	2.5585	0.0449
OpenVINS + Wheel	0.7388	0.6274	1.0562	0.0351

Compared with the baseline, the proposed method reduces RMSE by approximately 45%, Mean APE by 43%, and Max APE by 59%. Mean RPE is also reduced, indicating improved local motion consistency. These results are consistent with the role of wheel odometry as a complementary constraint in environments where visual tracking is weakened by repetitive structure and limited texture.

The estimated trajectories are shown in Fig. 5. Both methods recover the overall path, but the wheel-assisted configuration returns more consistently toward the starting point and exhibits less accumulated drift over the course of the run. This qualitative behavior agrees with the quantitative error reduction reported in Table II.

Fig. 3. Indoor corridor environment used in the experiments. The repetitive wall and floor patterns provide limited distinctive visual features for visual–inertial estimation.

Fig. 4. Outdoor environment used in the experiments. The scene provides richer visual texture and more distinctive features than the indoor corridor sequence.

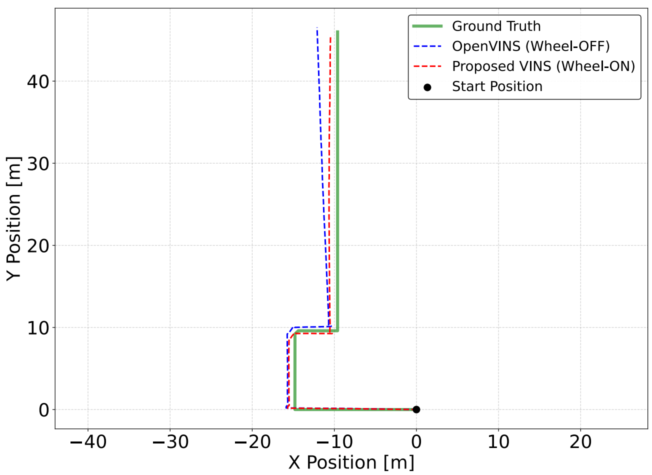

Fig. 5. Estimated trajectories for the indoor corridor experiment. The wheel-assisted configuration shows improved trajectory consistency and reduced drift relative to the baseline OpenVINS estimator.

B. Outdoor Results

The outdoor environment provides stronger visual constraints than the indoor corridor, so the baseline OpenVINS estimator already performs relatively well. Nevertheless, the results show that wheel odometry continues to provide a useful complementary constraint, with the magnitude of improvement depending on the motion profile.

Straight-Line Test: The outdoor straight-line experiment provides a controlled scenario for quantitative comparison. The estimated trajectories are shown in Fig. 6, and the corresponding error metrics are listed in Table III.

TABLE III

TRAJECTORY ERROR METRICS FOR THE 65-METER OUTDOOR STRAIGHT-LINE TEST

Method	RMSE	Mean APE	Max APE	Mean RPE
OpenVINS	0.1618	0.1287	0.4918	0.0060
OpenVINS + Wheel	0.1486	0.1184	0.4536	0.0053

The improvements in this test are modest but consistent across all metrics. RMSE decreases from 0.1618 m to 0.1486 m, while Mean APE, Max APE, and Mean RPE also show small reductions. This behavior is expected in a feature-rich outdoor environment, where visual constraints are already strong and the baseline estimator performs well. Even so, the results indicate that wheel odometry still contributes a measurable stabilizing effect.

Free-Form Path Test: In the second outdoor experiment, the robot followed a free-form path without an external reference trajectory. The comparison is therefore qualitative and is based on the geometric consistency of the estimated motion, as shown in Fig. 7.

A clear difference can be observed between the two configurations. The baseline OpenVINS trajectory exhibits noticeable drift and does not return close to the initial position at the end of the run. In contrast, the wheel-assisted configuration produces a trajectory with substantially better start–end consistency, indicating reduced drift accumulation over the full trajectory.

This result complements the straight-line test. While the straight-line scenario shows only modest quantitative improvement under favorable visual conditions, the free-form experiment reveals that wheel odometry becomes more valuable as the motion becomes longer and more varied. Taken together with the indoor results, the outdoor experiments support the conclusion that wheel odometry provides a meaningful complementary constraint across different environments and motion profiles.

Overall, the experiments show that the proposed integration improves OpenVINS most clearly when visual information is weak or when drift accumulates over longer trajectories. The gains are strongest in the indoor corridor sequence, modest but consistent in the outdoor straight-

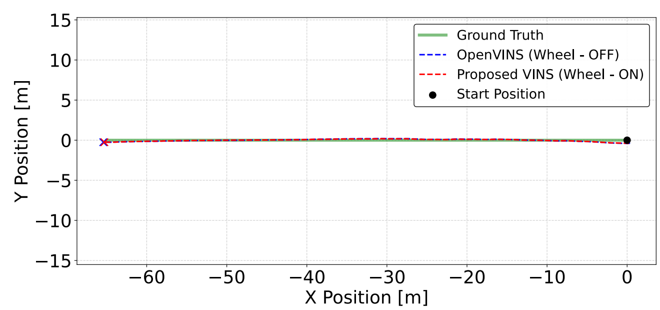

Fig. 6. Estimated trajectories for the outdoor straight-line experiment.

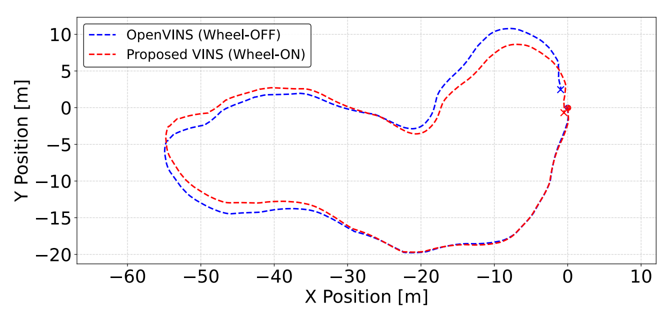

Fig. 7. Estimated trajectories for the outdoor free-form path experiment.

line test, and qualitatively significant in the outdoor free-form run. These findings support the main claim of the paper: wheel odometry can be incorporated into OpenVINS in a lightweight manner that improves robustness without modifying the estimator state.

VI. CONCLUSIONS

This paper presented a lightweight integration of wheel odometry into the OpenVINS visual–inertial odometry framework and validated the resulting system on a custom wheeled mobile robot. The proposed method incorporates wheel-derived motion information as an additional relative-motion update between consecutive MSCKF clone states, using RK4-based preintegration while preserving the original OpenVINS state representation. In contrast to approaches that increase estimator dimension or rely on heavier optimization back-ends, the proposed formulation retains the architectural simplicity and real-time computational profile of standard OpenVINS.

Experimental evaluation in both indoor and outdoor environments showed that the wheel-assisted configuration consistently improves estimation robustness relative to the baseline OpenVINS system. In the indoor corridor experiment, where repetitive structure and limited texture weaken visual constraints, the proposed method reduced the trajectory RMSE by approximately 45%, the mean absolute pose error by about 43%, and the maximum absolute pose error by nearly 59%. In the outdoor straight-line experiment, where visual conditions were more favorable, the improvement was smaller but remained consistent across all reported error metrics. In the outdoor free-form experiment, where no external reference trajectory was available, the wheel-assisted configuration produced substantially better trajectory closure and start–end consistency, indicating reduced drift accumulation over the full run.

Taken together, these results show that wheel odometry provides a practical and effective complementary sensing modality for visual–inertial estimation on wheeled ground robots. Its contribution is most evident when visual information is degraded or when drift accumulates over longer trajectories, but the experiments also show that it remains beneficial under favorable visual conditions. The main outcome of this work is therefore not only the validation of OpenVINS on a real robotic platform, but also the demonstration that meaningful robustness gains can be achieved through a minimally invasive wheel-assisted extension that does not require estimator-state augmentation.

Future work will focus on broader quantitative evaluation with external ground truth, testing under more aggressive motion and slip conditions, and investigating more explicit wheel-motion models that account for platform-dependent nonidealities. These directions would help further clarify the limits and practical deployment potential of lightweight wheel-assisted visual–inertial odometry for embedded robotic systems.

ACKNOWLEDGMENT

This work was supported by the Scientific and Technological Research Council of Türkiye (TÜBİTAK) under Grant No. 7240655 awarded to I.U. The authors thank TÜBİTAK 2210 program for Mehmet Muratoğlu's fellowship.

REFERENCES

[1] A. I. Mourikis and S. I. Roumeliotis, "A Multi-State Constraint Kalman Filter for Vision-Aided Inertial Navigation," in *Proc. IEEE Int. Conf. Robotics and Automation (ICRA)*, Rome, Italy, 2007, pp. 3565–3572.

[2] P. Geneva, K. Eckenhoff, W. Lee, Y. Yang, and G. Huang, "OpenVINS: A Research Platform for Visual-Inertial Estimation," in *Proc. IEEE Int. Conf. Robotics and Automation (ICRA)*, Paris, France, 2020, pp. 4666–4672.

[3] C. Campos, R. Elvira, J. J. Gomez Rodriguez, J. M. M. Montiel, and J. D. Tardos, "ORB-SLAM3: An Accurate Open-Source Library for Visual, Visual–Inertial, and Multimap SLAM," *IEEE Trans. Robot.*, vol. 37, no. 6, pp. 1874–1890, Dec. 2021.

[4] R. Buchanan, V. Agrawal, M. Camurri, F. Dellaert, and M. Fallon, "Deep IMU Bias Inference for Robust Visual-Inertial Odometry with Factor Graphs," *IEEE Robot. Autom. Lett.*, vol. 8, no. 1, pp. 41–48, Jan. 2023.

[5] Y. Liu, C. Zhao, and M. Ren, "An Enhanced Hybrid Visual–Inertial Odometry System for Indoor Mobile Robot," *Sensors*, vol. 22, no. 8, p. 2930, Apr. 2022.

[6] G. P. Huang, A. I. Mourikis, and S. I. Roumeliotis, "Observability-Based Rules for Designing Consistent EKF SLAM Estimators," *Int. J. Robot. Res.*, vol. 29, no. 5, pp. 502–528, 2010.

[7] J. Liu, W. Gao, and Z. Hu, "Visual-Inertial Odometry Tightly Coupled with Wheel Encoder Adopting Robust Initialization and Online Extrinsic Calibration," in *Proc. IEEE/RSJ Int. Conf. Intell. Robots Syst. (IROS)*, Macau, China, Nov. 2019, pp. 5391–5397.

[8] W. Lee, Y. Yang, and G. Huang, "Visual-Inertial-Wheel Odometry with Online Calibration," in *Proc. IEEE/RSJ Int. Conf. Intell. Robots Syst. (IROS)*, Las Vegas, NV, USA, Oct. 2020.

[9] A. Mandow, J. L. Martínez, J. Morales, J. L. Blanco, A. García-Cerezo, and J. González, "Experimental Kinematics for Wheeled Skid-Steer Mobile Robots," in *Proc. IEEE/RSJ Int. Conf. Intell. Robots Syst. (IROS)*, San Diego, CA, USA, Oct.–Nov. 2007, pp. 2845–2850.

[10] W. Lee, P. Geneva, C. Chen, and G. Huang, "MINS: Efficient and Robust Multisensor-Aided Inertial Navigation System," *arXiv preprint arXiv:2309.15390*, submitted for publication, 2023.

[11] Stereolabs, "ZED X Stereo Camera," [Online]. Available: `https://www.stereolabs.com/products/zed-x`, Accessed: 2025.

[12] Movella, "MTi 7 GNSS/INS Development Kit – User Manual," [Online]. Available: `https://www.movella.com/products/sensor-modules/xsens-mti-7`, Accessed: 2023.

[13] R. Buchanan, "Allan Variance ROS," Oxford Robotics Institute, DRS Lab, ver. 1.2, Nov. 2021. [Online]. Available: `https://github.com/ori-drs/allan_variance_ros`

[14] T. Moore and D. Stouch, "A Generalized Extended Kalman Filter Implementation for the Robot Operating System," in *Proc. 13th Int. Conf. Intell. Auton. Syst. (IAS-13)*, Padova, Italy, Jul. 2014.

[15] P. Furgale, J. Rehder, and R. Siegwart, "Unified Temporal and Spatial Calibration for Multi-Sensor Systems," in *Proc. IEEE/RSJ Int. Conf. Intell. Robots Syst. (IROS)*, Tokyo, Japan, 2013, pp. 1280–1286.

[16] T. Lupton and S. Sukkarieh, "Visual-Inertial-Aided Navigation for High-Dynamic Motion in Built Environments Without Initial Conditions," *IEEE Trans. Robot.*, vol. 28, no. 1, pp. 61–76, Feb. 2012.

[17] C. Forster, L. Carlone, F. Dellaert, and D. Scaramuzza, "On-Manifold Preintegration for Real-Time Visual–Inertial Odometry," *IEEE Trans. Robot.*, vol. 33, no. 1, pp. 1–21, Feb. 2017.

[18] G. P. Huang, A. I. Mourikis, and S. I. Roumeliotis, "A First-Estimates Jacobian EKF for Improving SLAM Consistency," in *Proc. 11th Int. Symp. Experimental Robotics (ISER)*, Athens, Greece, Jul. 2008, pp. 373–382.

[19] M. Li and A. I. Mourikis, "High-Precision, Consistent EKF-Based Visual–Inertial Odometry," *Int. J. Robot. Res.*, vol. 32, no. 6, pp. 690–711, May 2013.

[20] K. Belsare *et al.*, "Micro-ROS," in *Robot Operating System (ROS): The Complete Reference*, A. Koubaa, Ed. Cham, Switzerland: Springer, 2023, vol. 7, pp. 3–55.